Article

Geophysical imaging of the Yellowstone hydrothermal plumbing system

https://doi.org/10.1038/s41586-021-04379-1

Received: 17 March 2021

Accepted: 22 December 2021

Published online: 23 March 2022

Check for updates

Carol A. Finn[1]✉, Paul A. Bedrosian[1], W. Steven Holbrook[2], Esben Auken[3], Benjamin R. Bloss[1] & Jade Crosbie[1]

The nature of Yellowstone National Park's plumbing system linking deep thermal fluids to its legendary thermal features is virtually unknown. The prevailing concepts of Yellowstone hydrology and chemistry are that fluids reside in reservoirs with unknown geometries, flow laterally from distal sources and emerge at the edges of lava flows[1–4]. Here we present a high-resolution synoptic view of pathways of the Yellowstone hydrothermal system derived from electrical resistivity and magnetic susceptibility models of airborne geophysical data[5,6]. Groundwater and thermal fluids containing appreciable total dissolved solids significantly reduce resistivities of porous volcanic rocks and are differentiated by their resistivity signatures[7]. Clay sequences mapped in thermal areas[8,9] and boreholes[10] typically form at depths of less than 1,000 metres over fault-controlled thermal fluid and/or gas conduits[11–14]. We show that most thermal features are located above high-flux conduits along buried faults capped with clay that has low resistivity and low susceptibility. Shallow subhorizontal pathways feed groundwater into basins that mixes with thermal fluids from vertical conduits. These mixed fluids emerge at the surface, controlled by surficial permeability, and flow outwards along deeper brecciated layers. These outflows, continuing between the geyser basins, mix with local groundwater and thermal fluids to produce the observed geochemical signatures. Our high-fidelity images inform geochemical and groundwater models for hydrothermal systems worldwide.

The renowned hydrothermal system of Yellowstone National Park (YNP) results from shallow magma that supplies heat[3,15,16] and faults, kept open by active seismicity[17–19], that provide conduits for groundwater to circulate to deep, high-temperature regions and flow back to the surface as thermal fluids[3,8,20]. Three caldera-forming eruptions within the last 2.1 Ma (ref. [8]) have formed stacks of ash-flow tuffs and rhyolites on top of Tertiary volcanic rocks[8] that provide a layered stratigraphy conducive to lateral fluid flow (Fig. 1). Current models for the YNP hydrothermal system are based on geochemistry and the spatial relation between thermal features and surface geology. Permeable breccias[10,21] guide thermal fluid flow and localize thermal features at lava flow fronts[1,2,22]. Mixing of groundwater with steam and gas boiled out of deep alkaline waters creates acid-sulfate pools, fumaroles and mud pots[1,3].

Resistivity and susceptibility models

To map the YNP regional plumbing system, we inverted airborne electromagnetic (AEM) data[5] (Fig. 1) to generate one-dimensional (1D) electrical resistivity models to a maximum depth of 700 m (ref. [23]; Methods). The broad (100 m) footprint of the AEM system limits the lateral resolution of the models. Depth resolution is a complex function of subsurface resistivity, system altitude and depth[24]; on average, the depth resolution is 10–20 m from the surface to a depth of around 400 m and decreases with increasing depth. Conductive thermal features are mapped with higher resolution than resistive features. In addition, resolvable features must be larger than their depth. In most volcanic hydrothermal systems, characteristic sequences of hydrothermal clays overlie high-flux fluid or gas conduits such as faults and fractures[13,14,25]. These clay sequences often extend laterally for tens of kilometres and typically range from 200 to 1,500 m thick[11,14]. At YNP, these sequences are mapped in a few boreholes (Y-9 and Y-12)[10,26] and at the base of the Grand Canyon of the Yellowstone[9], and their contrasts in susceptibility with fresh volcanic rocks are the primary cause of the modelled low susceptibilities in YNP[27–29]. To map clays below the AEM depth resolution, we inverted YNP magnetic data[6] using a non-linear susceptibility inversion within a three-dimensional (3D) volume constrained by magnetic properties and depth weighting[30]. The maximum horizontal gradient of reduced-to-the-pole magnetic data filtered into different depth components[31] is used to identify deep fault fluid pathways (Methods).

Sections from the resistivity and magnetic susceptibility models provide the first views of fluid paths that compose the YNP regional plumbing system, and illustrate acid-sulfate (Figs. 1 and 2a, b, f (east side)) and neutral-chloride spring areas (Figs. 1 and 2c–e, f (west side)), and the thermal basins in faulted areas (Fig. 2a, b, f (east side)) and those between lava flows (Fig. 2c, d, f (west side)). On the basis of the magnetic and electrical properties[12,27] and the modelling of AEM and magnetic data from other volcanic regions[11,12,32,33], we differentiate unaltered and relatively dry rhyolite that is electrically resistive and magnetic (>450 Ω m and with susceptibility >0.025; note that susceptibility is

[1]US Geological Survey, Denver, CO, USA. [2]Virginia Tech, Blacksburg, VA, USA. [3]Aarhus University, Aarhus, Denmark. ✉e-mail: cfinn@usgs.gov

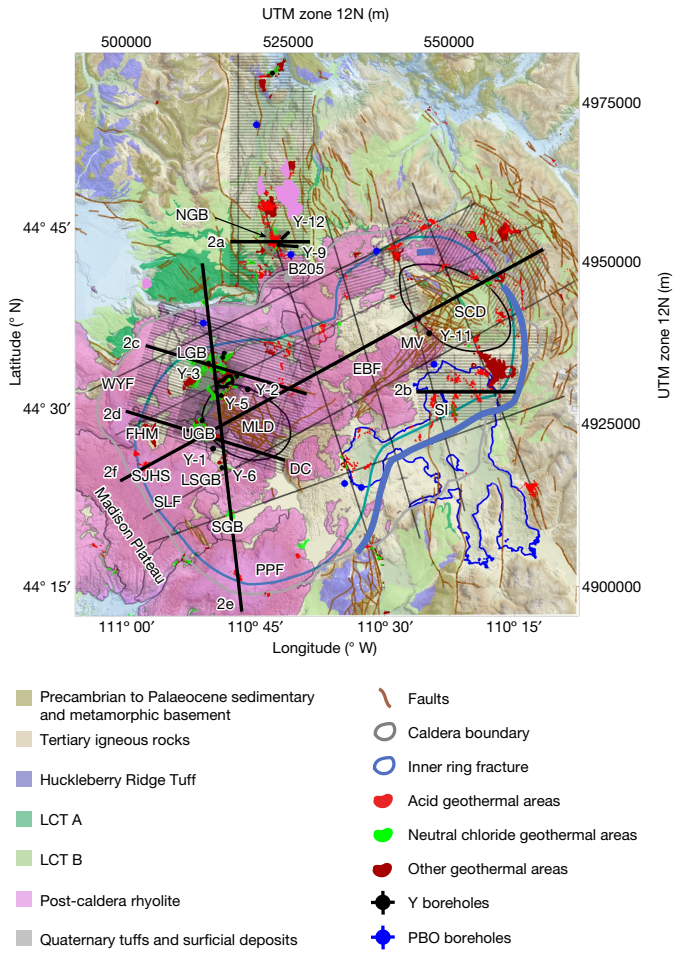

Fig. 1 | Grey-shade Digital Elevation Model overlain by a simplified geologic map of our study area in YNP. See YNP geologic map[8]. Black lines indicate cross sections shown in Fig. 2. Y (ref.[10]) and PBO (ref. [26]) boreholes are indicated by their numbers. Yellowstone Lake is outlined in blue. Labelled features include DeLacy Creek (DC); Elephant Back Flow (EBF); Firehole Meadows (FHM); Lone Star Geyser Basin (LSGB); Lower Geyser Basin (LGB); Mallard Lake Dome (MLD); Mud Volcano (MV); Norris Geyser Basin (NGB); Pitchstone Plateau Flow (PPF); Shoshone Geyser Basin (SGB); Smoke Jumper Hot Springs (SJHS); Stevenson Island (SI); Summit Lake Flow (SLF); Upper Geyser Basin (UGB); and West Yellowstone Flow (WYF).

dimensionless) from wet fresh rhyolite that is less resistive and still magnetic (approximately 15–450 Ω m and with susceptibility >0.025); we also identify substantial hydrothermal clay volumes from resistivities of less than approximately 15 Ω m and susceptibilities of less than approximately 33% of the fresh values[12] (here less than approximately 0.018). Water saturation and alteration are the primary factors in lowering resistivity, with the former controlled by lithology (for example, rhyolite flows and tuff versus breccia)[34] (Extended Data Fig. 1) and the latter by the degree and type of alteration. Although temperature lowers resistivity in the laboratory[35], in Yellowtone[34] and other volcanic hydrothermal basins[33] resistivity and temperature do not directly correlate (Methods).

The Norris Geyser Basin (NGB) lies in a fault-bounded block of Lava Creek Tuff (LCT A and B)[8] with resistivities ranging from approximately 7–150 Ω m; the higher values form discrete units separated by near vertical breaks probably corresponding to fracture networks along which fluids flow[36] (for example, Fig. 2a, red arrows). Resistivities of less than approximately 30 Ω m and low-to-moderate measured and modelled magnetic susceptibilities[27] indicate variable hydrothermal alteration of LCT, mostly along fractures. Modelled low susceptibilities are interpreted to represent the continuation of clays mapped in boreholes (for example, Y-12, Fig. 2a) below the NGB[27]. The LCT A–B boundary at Y-12 discharges hot water[10] (Fig. 2a, blue dashed line above LCT labels) and at Y-5 (Fig. 1) has high values of porosity and permeability[21]. Significant fluids flow at 5–7.6 l s^{-1} with conductivities of approximately 1,050 µS cm^{-1} (ref. [26]), typical of thermal springs[37] in the boundary at B205 (ref. [26]; Fig. 1). The resistivity of the A–B boundary at the location of Y-12 is approximately 30 Ω m (ref. [34]) and it increases away from the basin to moderate values of approximately 150–250 Ω m where the boundary is approximately 60 m thick (Fig. 2a). Evidence that these moderate resistivities reflect groundwater includes similar resistivities in thin (approximately 10 m) layers, for which the intersections with the surface coincide with cold springs[20] (Fig. 2a). Also, given Archie's Law[7] with measured porosities for the LCT A–B boundary[21] and typical groundwater conductivities[37], the expected resistivities correspond to the observed 150–250 Ω m range (Extended Data Fig. 1). At the base of LCT A, the approximately 5–50 Ω m resistivity layers indicate the presence of thermal fluids, but not significant alteration, as the susceptibilities remain high (Fig. 2a and Extended Data Fig. 1).

The NGB provides a model for the interaction of thermal fluids and groundwater throughout YNP. As thermal fluids (Fig. 2a, red lines) approach the edges of the NGB, they mix with groundwater (Fig. 2a, blue dashed lines) to form warm springs[38]. On both sides of the NGB, the LCT A–B boundaries intersect the basin in the subsurface, probably providing the groundwater input required by geochemical data to mix with thermal fluids rising along deep faults (Fig. 2a, brown lines) and shallow fractures in the centre of the basin. These mixed fluids flow out and down from the basin into a permeable zone at the base of LCT A, forming outflows (Fig. 2a, black dashed lines). Because the topographic gradient at the base of LCT A dips towards the NGB, outflow directions are difficult to determine (Fig. 2a). Small-scale fractures near the surface localize the hot springs[36] but are unresolved by our models.

Faults and fissures localize thermal features in the northern part of Yellowstone Lake, which has high heat flow[2,28] (Figs. 1 and 2b). Very low resistivities (<3 Ω m) in approximately 100-m-thick undulating layers (Fig. 2b) reflect pervasively altered[28] water-saturated clays within thermal fluid pathways. The flow of hot fluids along mapped faults localizes low-susceptibility clay sequences (Fig. 2b). A significant magnetic and heat-flow boundary, interpreted to represent a major structure[28] associated with fluid-generated earthquake swarms[17] (Fig. 2b, blue stars) corresponds to the western clay sequence.

The Lower Geyser Basin (LGB) and Upper Geyser Basin (UGB) (Figs. 1 and Fig. 2c, d) are bounded by resistive surficial rhyolite flows. In the LGB, low resistivities reflect intensely altered water saturated clays in the Elephant Back Flow (EBF, Y-2, Fig. 2c)[10,34], in contrast to more resistive and segmented layers associated with an older rhyolite flow to the west (unknown central plateau rhyolite flow, Y-3, Fig. 2c). A magnetic boundary (Fig. 2c) may represent a fault fluid conduit. In the UGB, the buried, altered Biscuit Basin Flow (BBF, Y-1, C-1, Fig. 2d)[10] has resistivities ranging from 3 to 50 Ω m (ref. [34]). Breaks in resistivity in the BBF (Fig. 2d) represent thermal fluid pathways. Low susceptibilities characterize the basin in much of the upper approximately 750 m, reflecting clays (Fig. 2c) as indicated in boreholes[10].

Shallow (less than around 130 m), thin (approximately 50 m), moderately resistive layers reflect groundwater in porous contacts between rhyolite lava flows (Extended Data Fig. 1) that drain into the LGB and UGB (Fig. 2c, d, blue lines) similar to the NGB (Fig. 2a). In some cases, resistivities decrease (to around 30–60 Ω m) beneath the edges of the lava flows, probably due to mixing of groundwater with thermal fluids (Fig. 2c, d). Below these layers, to the east and west of the LGB and UGB, are approximately 40-m-thick layers with resistivities of 10–30 Ω m, reflecting thermal fluid outflows (Fig. 2c, d) from the central conduits (Fig. 2c, d). Vertical resistivity discontinuities in buried flows

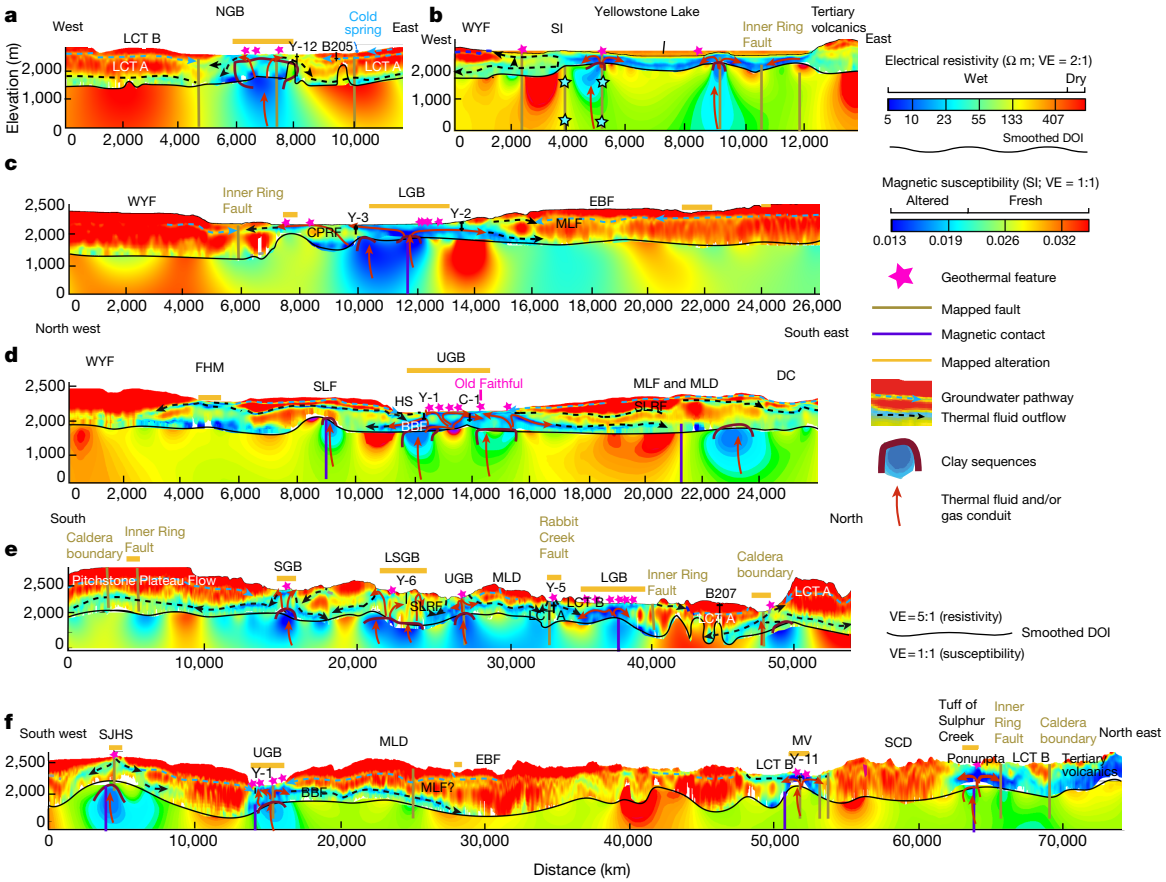

Fig. 2 | Cross sections from 1D resistivity (top of panel) and 3D susceptibility inverted models (bottom of panel) along selected profiles (locations in Fig. 1). Geologic and geothermal features from the YNP geologic map[8]; boreholes Y (ref. [10]) and B (ref. [26]). VE, vertical exaggeration. **a**, NGB. LCT A and LCT B. **b**, Northern Yellowstone Lake. Blue stars indicate locations of seismic swarms[17]. **c**, LGB. MLF, Mallard Lake Flow; CPRF, unknown central plateau rhyolite flow[10]. **d**, UGB. HS, Hillside Springs[38]. **e**, Geyser basins. SLRF, Scaup Lake rhyolite flow. **f**, Central caldera. SCD, Sour Creek Dome.

are observed beneath Firehole Meadows (FHM; Fig. 2d). Thermal fluids appear to flow from FHM to the UGB and under the West Yellowstone Flow (WYF). Low-susceptibility zones reflect inferred clay sequences near the proposed vent for the Mallard Lake Flow[8] and beneath the Summit Lake Flow that coincides with a magnetic contact reflecting a fault (Fig. 2d). Their relation, if any, to thermal fluids is unclear owing to the lack of depth resolution in the resistivity models.

In two long transects (Fig. 1), the lowest resistivities occur beneath (1) the geyser basins within the caldera (Figs. 1 and 2e), (2) the acid-sulfate-altered Mud Volcano and Tuff of Sulphur Creek (Ponunpta Spring) along the edges of the Sour Creek Dome (Fig. 2f) and (3) Tertiary volcanics (Fig. 2f). In general, thick (300–500 m) stacks of resistive lava flows, some of which contain groundwater, are underlain by low-resistivity layers related to thermal fluid paths. These fluids flow in the subsurface between the geyser basins (Fig. 2e) and emerge at the surface in gaps between the youngest lava flows. The central caldera is characterized by resistive rhyolite flows with shallow subhorizontal interfaces of moderate resistivity indicating groundwater in lava flow boundaries (Fig. 2e) but with little thermal fluid in the upper 700 m (Fig. 2f). Low-susceptibility clays occur below Smoke Jumper Hot Springs and the UGB but not beneath the central caldera nor Mud Volcano (Fig. 2f).

Yellowstone fluid pathways

On the basis of our cross sections and analogous with other geothermal areas[13,39–41], upflow zones are characterized by resistivities of less than approximately 15 Ω m and the observed hydrothermal activity (Figs. 2 and 3). These values can be slightly higher where clay alteration is not extensive (for example, the NGB, Figs. 2a and 3). Outflow zones are imaged as low-resistivity layers (approximately 15–30 Ω m) that are interpreted to contain thermal fluids that emanate from the upflow zones and negligible alteration (Fig. 2). To visualize the locations of the interpreted upflow and outflow zones, we extracted resistivities of less than 30 Ω m from the resistivity model (Fig. 3a). Where the fluid paths slope, we draw arrows to indicate potential flow directions. A section at a depth of 1,000 m from the susceptibility model clipped to less than 0.018 identifies the characteristic clay sequences interpreted to overlie the fault/fracture conduits for thermal fluids (Fig. 3b) (derived from mapping[8] and magnetic data (Methods)).

The upflow zones contain vertical and lateral thermal fluid pathways, clay layers, moderate to high fluid conductivities[37] and high temperatures[10]. Fluids rise along faults beneath the clay sequences[3,8,42] and spread laterally within basins and beneath adjacent lava flows as subsurface outflow zones (Figs. 2 and 3a). Geochemical models indicate that thermal fluids flow to the surface from reservoirs with temperatures in the range of 180–270 °C at depths of 100–550 m[3], where we image thermal fluids (Fig. 2). Outflow zones at depths of more than approximately 150 m often connect beneath mapped thermal areas. The lack of thermal fluids (Figs. 2f and 3a) and few clay sections in the central caldera (Fig. 3b) indicates that thermal fluids are absent or not ascending to the upper 1,000 m.

Shallow groundwater in lava flow boundaries enters most thermal areas, mixing with thermal fluids at the edges of basins in the subsurface. Geochemical models of the dilution of thermal fluids that feed surface features along the edges of some of the thermal basins supports our model of groundwater influx[3,4,10,20,38] (Figs. 2 and 3a). At the scale of

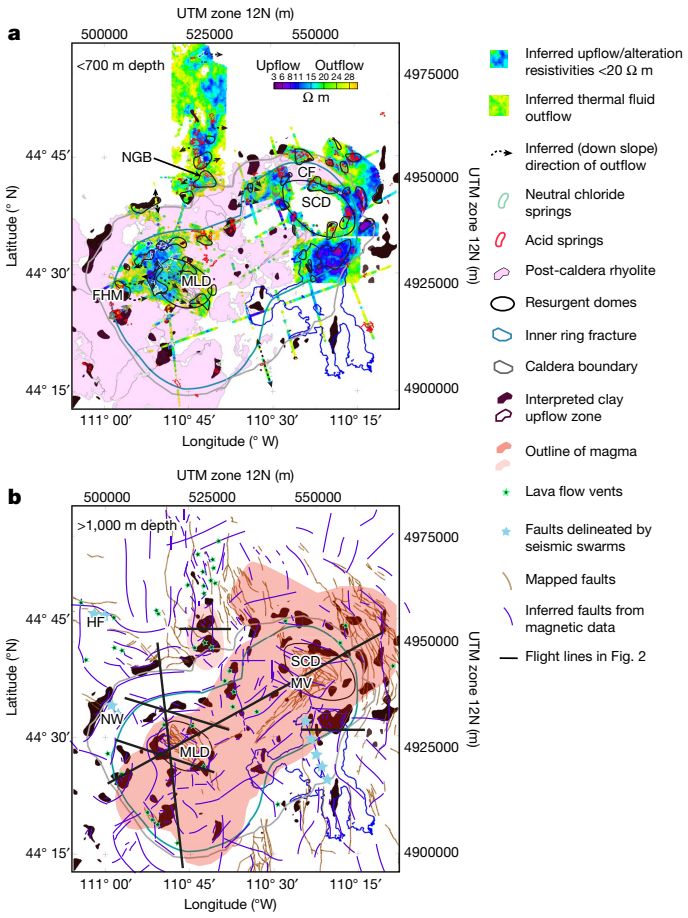

Fig. 3 | Plan view from resistivity and susceptibility inversions. a, Lateral extent of resistivities of less than 30 Ω m highlighting upflow and outflow regions. Susceptibilities from the voxel model of less than 0.18 at a depth of 1,000 m masked to eliminate sedimentary units. **b**, Mapped faults from geologic mapping[8]; faults delineated from seismic swarms (from Yellowstone Lake[17]; Hebgen Fault area (HF)[19]; and north west (NW) caldera boundary[18]); and inferred faults calculated from magnetic data (Methods). Labelled features include: Canyon Flow (CF); Fire Hole Meadows (FHM); Mallard Lake Dome (MLD); Mud Volcano (MV); Norris Geyser Basin (NGB) and Sour Creek Dome (SCD). Magma body locations from seismic tomography[15] and inferred from geochemistry for the NGB area[44].

our models, the thermal fluid pathways feeding neutral-chloride and acid-sulfate springs are similar, indicating that variations in spring chemistry are dominated by metre-scale structure and permeability variations beyond the resolution of our data .

Discrete low-susceptibility clay sequences ranging from 500 m to 5,000 m in width are modelled along the caldera rim and inner ring fracture, the edges of domes, the vent locations and the mapped faults or those inferred from magnetic contacts (Fig. 3b). The few small low-susceptibility regions in the central caldera line up along possible connections with the regional faults north and south of the caldera and with vent alignments. Low-susceptibility regions diminish north of the NGB (Fig. 3c) despite extensive faulting and lava flow vents, probably due to lower temperatures[10] that are insufficient to produce clay alteration. This relation of clay distribution, faults and thermal areas highlights the confluence of heat (magma), fractures/faults and fluids required to generate Yellowstone thermal features (Fig. 3b). Some of the low-susceptibility zones may relate to buried or palaeo-hydrothermal systems (for example, the dormant[43] Ponuntpa Spring, Fig. 2f), particularly those unassociated with modern thermal regions and far (>5 km) from the modern magma body (Figs. 2d and 3).

These high-resolution images reveal critical aspects of the Yellowstone hydrothermal system and can be used to assess geochemical models of the evolution of thermal fluids worldwide. Despite the inference of localization of thermal features by the lateral flow of thermal fluids into basins[1,2], we show that underlying most features are layers cut by vertical breaks and deeper thick sequences of clays that, along with mapped and magnetically identified faults, indicate vertical conduits for thermal fluids at depth. Locally, fluids from conduits travel beneath lava flows as outflows along brecciated boundaries that generally do not emerge at the surface except perhaps in the UGB (for example, Hillside Springs, Fig. 2d) and south of the southern caldera boundary (Fig. 3a). Where outflows from one basin intersect with a different basin, they mix with local thermal fluid upflow and groundwater, which is reflected in the diverse chemistry observed. The widespread distribution of the thermal fluids over much of the survey area, and inferred outside the caldera[19], indicates movement of these fluids away from various basins for long distances.

Online content

Any methods, additional references, Nature Research reporting summaries, source data, extended data, supplementary information, acknowledgements, peer review information; details of author contributions and competing interests; and statements of data and code availability are available at https://doi.org/10.1038/s41586-021-04379-1.

1. Hurwitz, S. & Lowenstern, J. B. Dynamics of the Yellowstone hydrothermal system. *Rev. Geophys.* **52**, 375–411 (2014).
2. Morgan, L. A., Shanks, W. C. & Pierce, K. L. Hydrothermal processes above the Yellowstone magma chamber: large hydrothermal systems and large hydrothermal explosions. *Geol. Soc. Am. Spec. Pap.* **459**, 1–95 (2009).
3. Fournier, R. O. Geochemistry and dynamics of the Yellowstone National Park hydrothermal system. *Annu. Rev. Earth Planet. Sci.* **17**, 13–53 (1989).
4. Truesdell, A. H., Nathenson, M. & Rye, R. O. The effects of subsurface boiling and dilution on the isotopic compositions of Yellowstone thermal waters. *J. Geophys. Res.* **82**, 3694–3704 (1977).
5. Finn, C. A., Bedrosian, P. A., Bloss, B. R., Holbrook, W. S. & Auken, E. Airborne electromagnetic and magnetic survey, Yellowstone National Park, 2016 – minimally processed data. *US Geol. Surv. ScienceBase Data Release* https://doi.org/10.5066/P9MCJ9B6 (2021).
6. US Geological Survey. An Aeromagnetic Survey in Yellowstone National Park: a web site for distribution of data (on-line edition). *US Geol. Surv. Open-File Report 00-163* https://pubs.usgs.gov/of/2000/ofr-00-0163/ (2000).
7. Archie, G. E. The electrical resistivity log as an aid in determining some reservoir characteristics. *Trans. Am. Inst. Min. Metall. Petrol. Eng.* **146**, 54–62 (1942).
8. Christiansen, R. L. The quaternary and pliocene Yellowstone Plateau volcanic field of Wyoming, Idaho, and Montana. *US Geol. Surv. Prof. Pap.* **729-G**, G1–G150 (2001).
9. Livo, K. E., Kruse, F. A., Clark, R. N., Kokaly, R. F. & Shanks III, W. *US Geol. Surv. Prof. Pap.* **1717**, 493–507 (2007).
10. White, D. E., Fournier, R. O., Muffler, L. J. P. & Truesdell, A. H. Physical results of research drilling in thermal areas of Yellowstone National Park, Wyoming. *US Geol. Surv. Prof. Pap.* **892**, 70 (1975).
11. Bibby, H., Caldwell, T., Davey, F. & Webb, T. Geophysical evidence on the structure of the Taupo Volcanic Zone and its hydrothermal circulation. *J. Volcanol. Geotherm. Res.* **68**, 29–58 (1995).
12. Hochstein, M. P. & Soengkono, S. Magnetic anomalies associated with high temperature reservoirs in the Taupo Volcanic Zone (New Zealand). *Geothermics* **26**, 1–24 (1997).
13. Rowland, J. & Sibson, R. Structural controls on hydrothermal flow in a segmented rift system, Taupo Volcanic Zone, New Zealand. *Geofluids* **4**, 259–283 (2004).
14. Simmons, S. F., White, N. C. & John, D. A. in *Economic Geology, One Hundredth Anniversary Volume* (eds Hedenquist, J. W. et al.) 485–522 (Society of Economic Geology, 2005).
15. Farrell, J., Smith, R. B., Husen, S. & Diehl, T. Tomography from 26 years of seismicity revealing that the spatial extent of the Yellowstone crustal magma reservoir extends well beyond the Yellowstone caldera. *Geophys. Res. Lett.* **41**, 3068–3073 (2014).
16. Nordstrom, D. K., McCleskey, R. B. & Ball, J. W. Sulfur geochemistry of hydrothermal waters in Yellowstone National Park: IV Acid–sulfate waters. *Appl. Geochem.* **24**, 191–207 (2009).
17. Farrell, J., Smith, R. B., Taira, T. A., Chang, W. L. & Puskas, C. M. Dynamics and rapid migration of the energetic 2008–2009 Yellowstone Lake earthquake swarm. *Geophys. Res. Lett.* **37**, 19305–19309 (2010).
18. Shelly, D. R. & Hardebeck, J. L. Illuminating faulting complexity of the 2017 Yellowstone Maple Creek earthquake swarm. *Geophys. Res. Lett.* **46**, 2544–2552 (2019).
19. Waite, G. P. & Smith, R. B. Seismic evidence for fluid migration accompanying subsidence of the Yellowstone caldera. *J. Geophys. Res. Solid Earth* **107**, 1–15 (2002). ESE 1-1-ESE.
20. Gardner, W. P., Susong, D. D., Solomon, D. K. & Heasler, H. P. A multitracer approach for characterizing interactions between shallow groundwater and the hydrothermal system in the Norris Geyser Basin area, Yellowstone National Park. *Geochem. Geophys. Geosystems* **12** (2011).

21. Dobson, P. F., Kneafsey, T. J., Hulen, J. & Simmons, A. Porosity, permeability, and fluid flow in the Yellowstone geothermal system, Wyoming. *J. Volcanol. Geotherm. Res.* **123**, 313–324 (2003).
22. Bouligand, C. et al. Heat and mass transport in a vapor-dominated hydrothermal area in Yellowstone National Park, USA: Inferences from magnetic, electrical, electromagnetic, subsurface temperature, and diffuse CO2 flux measurements. *J. Geophys. Res. Solid Earth* **124**, 291–309 (2019).
23. Bedrosian, P. et al. Airborne electromagnetic survey processed data and models data release, Yellowstone National Park, Wyoming, 2016. *US Geol. Surv. ScienceBase Data Release* https://doi.org/10.5066/P9LVAU7W (2021).
24. Auken, E., Christiansen, A. V., Jacobsen, L. & Sørensen, K. I. A resolution study of buried valleys using laterally constrained inversion of TEM data. *J. Appl. Geophys.* **65**, 10–20 (2008).
25. Munoz, G. Exploring for geothermal resources with electromagnetic methods. *Surv. Geophys.* **35**, 101–122 (2014).
26. Jaworowski, C. et al. Geologic and geochemical results from boreholes drilled in Yellowstone National Park, Wyoming, 2007 and 2008. *US Geol. Surv. Open-File Report* **2016-1029**, 1–38 (2016).
27. Bouligand, C., Glen, J. M. & Blakely, R. J. Distribution of buried hydrothermal alteration deduced from high-resolution magnetic surveys in Yellowstone National Park. *J. Geophys. Res. Solid Earth* **119**, 2595–2630 (2014).
28. Bouligand, C. et al. Geological and thermal control of the hydrothermal system in northern Yellowstone Lake: inferences from high resolution magnetic surveys. *J. Geophys. Res. Solid Earth* **125**, e2020JB019743 (2020).
29. Finn, C. A. & Morgan, L. A. High-resolution aeromagnetic mapping of volcanic terrain, Yellowstone National Park. *J. Volcanol. Geotherm. Res.* **115**, 207–231 (2002).
30. Phillips, J. D. Using vertical Fourier transforms to invert potential-field data to magnetization or density models in the presence of topography. *SEG Technical Program Expanded Abstracts* https://doi.org/10.1190/segam2014-0226.1 (2014).
31. Phillips, J. D. Designing matched bandpass and azimuthal filters for the separation of potential-field anomalies by source region and source type. *ASEG Extended Abstracts* https://doi.org/10.1071/ASEG2001ab110 (2001).
32. Finn, C. A., Deszcz-Pan, M., Ball, J. L., Bloss, B. J. & Minsley, B. J. Three-dimensional geophysical mapping of shallow water saturated altered rocks at Mount Baker, Washington: Implications for slope stability. *J. Volcanol. Geotherm. Res.* **357**, 261–275 (2018).
33. Hersir, G. P. & Arnason, K. Resistivity of rocks. In *Short Course IX on Exploration for Geothermal Resources* 1–8 (United Nations University, Geothermal Development Company and Kenya Electricity Generating Co., 2014).
34. Dickey, K. A. *Geophysical Investigation of the Yellowstone Hydrothermal System*. MS thesis, Virginia Polytechnical Institute (2018).
35. Llera, F. J., Sato, M., Nakatsuka, K. & Yokoyama, H. Temperature dependence of the electrical resistivity of water saturated rocks. *Geophysics* **55**, 576–585 (1988).
36. Jaworowski, C., Heasler, H. P., Hardy, C. C. & Queen, L. P. Control of hydrothermal fluids by natural fractures at Norris Geyser Basin. *Yellowstone Sci.* **14**, 13–23 (2006).
37. McCleskey, R. et al. Water-chemistry data for selected springs, geysers, and streams in Yellowstone National Park, Wyoming, Beginning 2009. *US. Geolog. Surv. Water Resources* https://doi.org/10.5066/F7M043FS (2014).
38. Gardner, W. P., Susong, D. D., Solomon, D. K. & Heasler, H. P. Using environmental tracers and numerical simulation to investigate regional hydrothermal basins—Norris Geyser Basin area, Yellowstone National Park, USA. *J. Geophys. Res. Solid Earth* **118**, 2777–2787 (2013).
39. Allis, R. Geophysical anomalies over epithermal systems. *J. Geochem. Explor.* **36**, 339–374 (1990).
40. Bibby, H. M., Dawson, G. B., Rayner, H. H., Bennie, S. L. & Bromley, C. J. Electrical resistivity and magnetic investigations of the geothermal systems in the Rotorua area, New Zealand. *Geothermics* **21**, 43–64 (1992).
41. Hedenquist, J. W., Goff, F., Phillips, F. M., Elmore, D. & Stewart, M. K. Groundwater dilution and residence times, and constraints on chloride source, in the Mokai geothermal system, New Zealand, from chemical, stable isotope, tritium, and 36Cl data. *J. Geophys. Res. Solid Earth* **95**, 19365–19375 (1990).
42. Farrell, J., Husen, S. & Smith, R. B. Earthquake swarm and b-value characterization of the Yellowstone volcano-tectonic system. *J. Volcanol. Geotherm. Res.* **188**, 260–276 (2009).
43. Vaughan, R. G., Heasler, H., Jaworowski, C., Lowenstern, J. B. & Keszhelyi, L. P. Provisional maps of thermal areas in Yellowstone National Park, based on satellite thermal infrared imaging and field observations. *U.S. Geol. Surv. Scientific Investigations Report* **2014-5137**, 1–22 (2014).
44. White, D. E., Hutchinson, R. A. & Keith, T. E. The geology and remarkable thermal activity of Norris Geyser basin, Yellowstone National Park, Wyoming. *US Geol. Surv. Prof. Pap.* **1456**, 1–84 (1988).

Methods

AEM and magnetic data

Airborne electromagnetic (AEM) and magnetic survey data were collected along 4,212 line kilometres over YNP, Wyoming[5] (Fig. 1). Data were acquired with the SkyTEM 312M time-domain helicopter-borne electromagnetic system. The survey was taken over several flight blocks with line spacing between 250 and 450 m and a series of regional reconnaissance caldera lines with 5 km nominal line spacing. Sensor position, altitude and attitude were all recorded; the mean instrument flight height was 48 m. Aeromagnetic data were flown over the entire park along east–west trending flight lines spaced 400 m apart, with north–south trending tie lines every 4 km at a mean flight elevation of approximately 245 m above ground in 1999 [6]. The magnetic data were sensitive to thousands of metres.

Resistivity processing and modelling

The AEM data were processed using the Aarhus Workbench software package (https://www.aarhusgeosoftware.dk/). Filters were applied to altimeter, inclinometer and spatial-positioning data to smooth raw data and remove sensor drop-outs. AEM data contaminated by coupling to known infrastructure (such as power lines, pipelines and buildings) were manually removed. Culled AEM data were averaged using an along-line trapezoidal filter of width from 30 to 180 m for early to late times, respectively, and soundings were exported with a 30 m interval. Late-time data with low signal-to-noise levels were removed through a combination of filters and manual culling.

Deterministic laterally constrained 1D inverse models of the processed AEM data were generated using the AarhusInv inversion kernel[45]. The effects of the residual primary field were modelled during the inversion to recover the near-surface resistivity structure[46]. For each sounding, data from 4.2 μs to 10.7 ms were inverted to determine a 30-layer smoothing-regularized inverse model starting from the best-fitting half-space model. Models were parameterized with fixed-layer depths ranging from 5 to 700 m and with logarithmically increasing layer thickness (Extended Data Table 1). When data sensitivity was low, most commonly at depths in excess of 300 m, adjacent models were constrained to be similar by having lateral constraints on resistivity that scale with the inverse distance between soundings[47]. System altitude was treated as a free parameter but with a tight standard deviation centred about the measured altitude. Applying a wide range of inversion parameters (model discretization, start-model resistivity, lateral constraints and altitude constraints) produced similar models, all of which contained the primary interpreted model features (Figs. 2 and 3). Differences between models were largely in the sharpness of the interfaces, the resistivity contrasts between layers and the model structures below a depth of 400 m. In addition, there were trade-offs between layer thickness and conductivity (equivalent conductivity-thickness product), an inability to resolve thin resistive layers and limited sensitivity to resistivity at the high end of the spectrum (for example, 1,000 versus 5,000 Ω m). The final inversion parameters (Extended Data Table 1) were selected as they best represented the physical characteristics of the AEM system and minimized data misfit. A cumulative sensitivity-based depth of investigation (DOI) was calculated for each inverse model[48] and this provided a relative measure of those parts of the model domain that were well constrained by the AEM data. The generalized DOI is indicated in Fig. 2 by the wavy black lines between the resistivity and susceptibility sections. The DOI had a mean value of approximately 450 m over the survey area, but ranged from approximately 125 m in highly conductive areas (for example, Yellowstone Lake) to more than 700 m over resistive areas (for example, the rhyolite flows over the central caldera). Lateral and vertical resolution was highly dependent on the conductivity of the subsurface[49] but in broad terms the lateral resolution was of the order of one hundred metres near to the surface to several hundred meters at depth, with the vertical resolution ranging from approximately 10 m near the surface to values in excess of 50 m at a depth of 700 m. The higher the conductivity, the more focused the electromagnetic fields and the better the resolution.

Susceptibility modelling

To model the susceptibility, we applied a non-linear inversion based on the Fourier transform relationship between the susceptibility distribution within a 3D volume and its corresponding magnetic field[30]. This problem is non-unique, so constraints such as depth weighting, positivity or a priori physical property models are applied to provide geologically reasonable solutions[30]. As we expect the largest susceptibility contrasts between magnetic and hydrothermally altered volcanic rocks to arise in the upper approximately 1–2 km (ref. [8]), the models were weighted to emphasize shallow contrasts. The topography bounded the top of the models and a flat surface at the approximate average Curie depth of around −5,000 m elevation[50] bounded the bottom. We tried several values for the bottoms to the models between 0 m elevation (the probable thinnest reasonable model given our estimate of the combined approximately 2,500 m thickness of the magnetic Tertiary and Cenozoic volcanic rocks[8]) and −10,000 m elevation, which is the deepest estimate of the Curie depth[50]. All models show similar distributions of high and low susceptibility for the depths over which they overlap. Comparison of a variety of models with different base elevations and cell sizes indicates consistency above 0 m elevation. We trimmed our model with a base elevation of −5,000 m to 0 m elevation, to focus on the most reliable portions of the model (Fig. 2). Magnetic susceptibilities and the thickness of lava flows vary widely and are poorly constrained by our models. The upper 250–500 m of the magnetic susceptibility model is quite variable and unreliable, which is probably related to the fact that we approximated the top surface with voxel blocks instead of having a smoothly varying topographic surface (Fig. 2). Therefore, we use the resistivity model at the top of the cross sections and the susceptibility model beneath (Fig. 2).

We assumed that the rocks are magnetized in the present Earth field direction with an inclination of 70° and a declination of 14°, which is a reasonable assumption for the LCT and younger rhyolites that are the focus of this study[27,29]. As the remanent and induced field directions are similar for the primary regions of interest, susceptibilities were used in the models rather than magnetization for ease of computation. Multiplying the measured susceptibility values by the typical range of the Koenigsberger ratios (2–24) for YNP volcanic rocks[27,29] and averaging yields a value of approximately 0.025, which we used as a starting value in the inversion. The final models contained individual voxel elements that display 3D physical property volumes of magnetic susceptibility. We used several voxel dimensions. For the entire park, the voxel size was $250 \times 250 \times 250$ m^3 (Figs. 2e, f and Fig. 3). For local areas, we cut down the size of the area and reduced the voxel dimensions to $80 \times 80 \times 80$ m^3 (Figs. 2a–d) to capture more detail. The susceptibilities in the voxel models ranged from 0.0002 to −0.11. The resulting root-mean-square error was less than 1 nT for all models. Due to uncertainties in thickness and susceptibility, the vertical resolution is poor.

To highlight shallow (the upper approximately 1–2 km) regions of hydrothermal clays in the map view for the entire park (Fig. 3), we isolated regions that had significantly lower susceptibilities than the adjacent rocks (generally less than 33% of the mean value of approximately 0.057) because we did not expect a rock mass to be completely altered at zero susceptibility and models and measurements on cores indicate that a reduction of 33% or more identifies alteration[32]. We masked out regions associated with magnetite-poor sedimentary units outside of the caldera. We show these isolated susceptibilities at 1,000 m depth, which is the approximate depth limit of hydrothermal clay assemblages seen elsewhere[13,14] (Fig. 3).

Magnetic contact determinations

To map magnetic contacts that image faults at varying depths, we used several methods. First, we separated the aeromagnetic data into several depth components, based on the match of the anomaly widths to anomalies produced by layers of hypothetical magnetic sources at different depths[31]. The data were separated into three components with the middle layer at a depth of approximately 1,000–5,000 m used in the magnetic contact calculations to identify potential deep conduits for fluids. Faults and fractures commonly produce linear crests in the horizontal gradients of the aeromagnetic data, so the next step was to apply a maximum horizontal gradient function to the filtered aeromagnetic data layers, which resulted in peaks over the contacts[51]. We digitized the major linear contacts likely to represent faults, eliminating the lava flow boundaries (Fig. 3).

Using Archie's Law to differentiate groundwater from thermal fluids

Deriving hydrogeologic information from electrical resistivity is non-trivial as resistivity in fresh volcanic rocks is controlled by generally poorly constrained parameters of lithology, porosity (or water content) and water quality that is reflected in the conductivity data. In addition to the observations discussed in the Article, we also interpret the resistivity models (Figs. 2 and 3a) based on Archie's Law for fully saturated rocks in the absence of clay (that is, fresh volcanic rocks)[7] (bulk resistivity = fluid resistivity × porosity$^{-\text{cementation factor}}$) with a cementation constant (reflecting the lithology) of 2.4, which is typical for fresh volcanic rocks[52] (Extended Data Fig. 1). These relations do not apply in the hydrothermally altered basins because of the high clay content. Given the high precipitation and borehole evidence[10,26] for water at depth, an assumption of complete water saturation is reasonable. Porosities are derived from borehole measurements in representative rock types for YNP[21,53,54] and water quality (conductivity) is based on surface[37] and borehole[26] measurements (Extended Data Fig. 1). For example, the observed bulk resistivities in our models of the LCT outside of the NGB (Figs. 2a and 3a) and comparison of the measured porosities of the LCT[21] with fluid conductivities typical for groundwater[26,37] show that the shallow, moderate resistivity (150–300 Ω m) layer in LCT B and the LCT A–B boundary (Fig. 2a) can relate to conductivities of less than 200 μS cm^{-1} with porosities of more than 0.25 and conductivities of thermal water if porosities are less than 0.25. Because the porosities in the LCT A–B boundary are in weakly welded LCT (porosity = 0.4 (ref. [21]), Extended Data Fig. 1) and clay is not extensive[27], groundwater is the likely source of the observed resistivities. At the base of LCT A, where the resistivities range from 5 to 50 Ω m, water with conductivities that exceed 800 μS cm^{-1} (a thermal fluid signature) is required to match the modelled bulk resistivities (Extended Data Fig. 1). These relations do not hold if there is significant clay; however, this is unlikely given the high susceptibilities and resistivities of more than 30 Ω m.

For the measured porosities in brecciated rhyolites and pumiceous tuff observed in Y-2 (ref. [53]) and Y-3 (ref. [54]) (Figs. 1, 2e and Extended Data Fig. 1), which we assume are similar to those outside of the geyser basins, the modelled 150–300 Ω m resistivity layers in the WYF and EBF relate to groundwater (Fig. 2e and Extended Data Fig. 1) as in the NGB (Fig. 2a). Along with other constraints, we use these rationales to differentiate groundwater from thermal fluids, recognizing significant variability in the porosities and conductivities. Although variations in fluid conductivity and lithology can fully explain the differences in model resistivity, temperature can also have an effect, potentially decreasing the resistivity by factors of 6–10 in the 30–250 °C temperature range[35]. For example, if the increase in resistivity from about 25 to 250 Ω m for the thermal fluid flowing outwards from Smoke Jumper Hot Springs (Fig. 2f, black dashed lines) were solely due to decreasing temperature away from the vent, an approximately 150 °C decrease in temperature based on laboratory studies is estimated[35]. However, measured fluid conductivities from the thermal fluids in Smoke Jumper Hot Springs can exceed 1,000 μS cm^{-1}, and that of the groundwater is less than 200 μS cm^{-1} (ref. [37]), so the increase in resistivity away from the vent can be wholly explained by decreases in fluid conductivity (Extended Data Fig. 1), rendering the temperature estimate a maximum. In addition, alteration sequences reflect their formation temperatures[13,14,53,54] and are associated with characteristic resistivites[11,40] regardless of the current temperature regime. For example, the resistivities beneath the active and hot Mud Volcano are similar to those of the dormant Ponuntpa Spring (Fig. 2f), indicating that temperature is a negligible resistivity effect relative to the other factors discussed here.

Data availability

The electromagnetic data[5] and models[23] and magnetic[6] data are freely available.

45. Auken, E. et al. An overview of a highly versatile forward and stable inverse algorithm for airborne, ground-based and borehole electromagnetic and electric data. *Explor. Geophys.* **46**, 223–235 (2015).
46. Schamper, C., Auken, E. & Sørensen, K. Coil response inversion for very early time modelling of helicopter-borne time-domain electromagnetic data and mapping of near-surface geological layers. *Geophys. Prospect.* **62**, 658–674 (2014).
47. Auken, E., Christiansen, A. V., Jacobsen, B. H., Foged, N. & Sørensen, K. I. Piecewise 1D laterally constrained inversion of resistivity data. *Geophys. Prospect.* **53**, 497–506 (2005).
48. Christiansen, A. V. & Auken, E. A global measure for depth of investigation. *Geophysics* **77**, WB171–WB177 (2012).
49. Christensen, N. B. Sensitivity functions of transient electromagnetic methods. *Geophysics* **79**, E167–E182 (2014).
50. Bhattacharyya, B. & Leu, L. K. Analysis of magnetic anomalies over Yellowstone National Park: mapping of Curie point isothermal surface for geothermal reconnaissance. *J. Geophys. Res.* **80**, 4461–4465 (1975).
51. Cordell, L. & Grauch, V. J. S. in *The Utility of Regional Gravity and Magnetic Anomaly Maps* (ed. Hinze, W. J.) 181–197 (Society of Exploration Geophysicists, 1985).
52. Revil, A. et al. Induced polarization of volcanic rocks–1. Surface versus quadrature conductivity. *Geophys. J. Int.* **208**, 826–844 (2016).
53. Bargar, K. E. & Beeson, M. H. Hydrothermal alteration in research drill hole Y-2, Lower Geyser Basin, Yellowstone National Park, Wyoming. *Am. Mineral.* **66**, 473–490 (1981).
54. Bargar, K. E. & Beeson, M. H. Hydrothermal alteration in research drill hole Y-3, Lower Geyser Basin, Yellowstone National Park, Wyoming. *US Geol. Surv. Prof. Pap.* **1054-C**, C1–C23 (1985).
55. Bargar, K. E. & Beeson, M. H. Hydrothermal alteration in research drill hole Y-6, Upper Firehole River, Yellowstone National Park, Wyoming. *US Geol. Surv. Prof. Pap.* **1054-B**, B1–B24 (1984).

Acknowledgements We thank B. Minsley for generating Extended Data Fig. 1 and S. Hurwitz and P. Gardner for suggestions that improved this paper. This work was supported by the US Geological Survey Mineral and Energy Resources and Volcanic Hazards Programs, NSF grant no. EPS-1208909 and the University of Wyoming Office of Research and Economic Development. This work was carried out when one of the co-authors, E.A., was a professor in geophysics at Aarhus University. Any use of trade, firm or product names is for descriptive purposes and does not imply endorsement by the US Government.

Author contributions C.A.F., P.A.B., W.S.H. and E.A. initiated the study and designed the AEM survey. C.A.F. modelled the magnetic data. P.A.B. and J.C. modelled the AEM data. C.A.F. and P.A.B. developed the interpretation with contributions from W.S.H., E.A., B.R.B. and J.C. C.A.F. wrote the bulk of the paper with P.A.B., W.S.H. and E.A. contributing.

Competing interests The authors declare no competing interests.

Additional information

Supplementary information The online version contains supplementary material available at https://doi.org/10.1038/s41586-021-04379-1.

Correspondence and requests for materials should be addressed to Carol A. Finn.

Peer review information *Nature* thanks William Gardner, Steven Constable and the other, anonymous, reviewer(s) for their contribution to the peer review of this work. Peer reviewer reports are available.

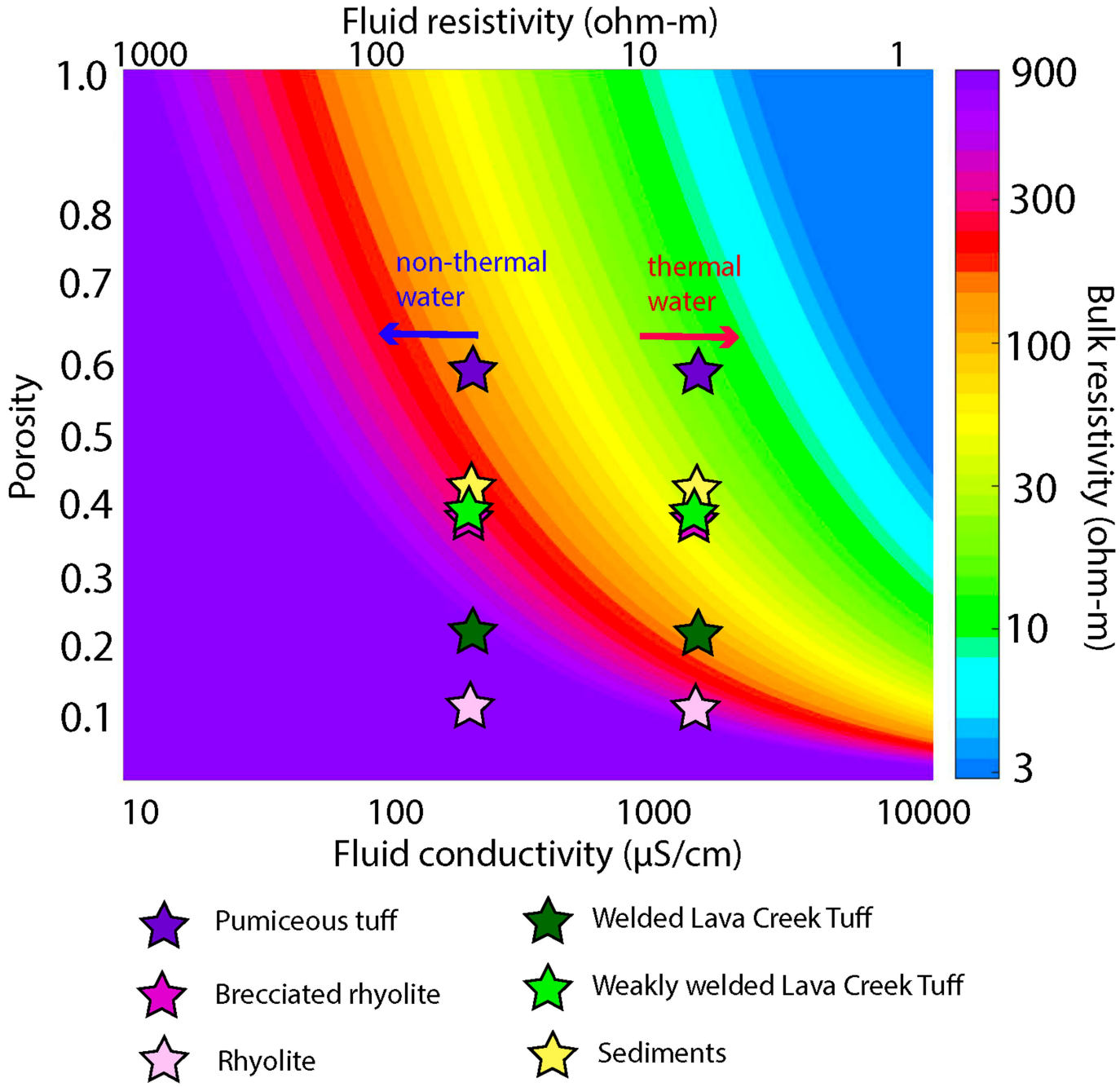

Extended Data Fig. 1 | Graph of bulk resistivity depending on porosity[21,53–55] and fluid conductivity[26,37]. The stars represent the maximums of measured porosity values[21,53–55], the highest values of fluid conductivities of groundwater and typical values for thermal fluids. The colors indicate the bulk resistivity values expected in our models (Figs. 2 and 3a) for given porosities and conductivities.

Extended Data Table 1 | AEM inversion parameters

Inversion Parameter	Value
low-moment time gates (26)	4.2 µs - 1.4 ms
high-moment time gates (27)	63 µs – 10.7 ms
# of model layers	30
Vertical layer discretization	Logarithmically increasing with depth
1st layer thickness (m)	5
last interface depth (m below land surface)	700
start model resistivity	Best-fitting halfspace model
vertical resistivity constraints	4.0 (extremely loose, corresponds to 400%)
lateral resistivity constraints	1.6 (very loose, corresponds to 60%)
altitude standard deviation (m)	1.0 (very tight)
altitude lateral constraints	1.1 (loose, corresponds to 10%
Further details can be found at http://www.ags-cloud.dk/Wiki/W_InversionGuides	